The broadening of the main sequence in the open cluster M38

M. Griggio [1,2]★ M. Salaris,[3,4] L. R. Bedin [2] and S. Cassisi[4,5]

[1]*Dipartimento di Fisica, Università di Ferrara, Via Giuseppe Saragat 1, I-44122 Ferrara, Italy*
[2]*INAF – Osservatorio Astronomico di Padova, Vicolo dell'Osservatorio 5, I-35122 Padova, Italy*
[3]*Astrophysics Research Institute, Liverpool John Moores University, 146 Brownlow Hill, Liverpool L3 5RF, UK*
[4]*INAF – Osservatorio Astronomico di Abruzzo, Via M. Maggini, I-64100 Teramo, Italy*
[5]*INFN – Sezione di Pisa, Largo Pontecorvo 3, I-56127 Pisa, Italy*

ABSTRACT

Our recent multiband photometric study of the colour width of the lower main sequence of the open cluster M37 has revealed the presence of a sizeable initial chemical composition spread in the cluster. If initial chemical composition spreads are common amongst open clusters, this would have major implications for cluster formation models and the foundation of the chemical tagging technique. Here, we present a study of the unevolved main sequence of the open cluster M38, employing *Gaia* DR3 photometry and astrometry, together with newly acquired *Sloan* photometry. We have analysed the distribution of the cluster's lower main-sequence stars with a differential colour–colour diagram made of combinations of *Gaia* and *Sloan* magnitudes, like in the study of M37. We employed synthetic stellar populations to reproduce the observed trend of M38 stars in this diagram and found that the observed colour spreads can be explained simply by the combined effect of differential reddening across the face of the cluster and the presence of unresolved binaries. There is no need to include in the synthetic sample a spread of initial chemical composition as instead necessary to explain the main sequence of M37. Further photometric investigations like ours, as well as accurate differential spectroscopic analyses on large samples of open clusters, are necessary to understand whether chemical abundance spreads are common among the open cluster population.

Key words: techniques: photometric – stars: abundances – binaries: general – open clusters and associations: individual: M38.

1 INTRODUCTION

Open clusters have been traditionally considered to host populations of stars born all with the same initial chemical composition in a burst of star formation of negligible duration (simple stellar populations).

The recent discovery of extended turn-offs (TOs) in the *Gaia* colour–magnitude diagrams (CMDs) of a sample of about 15 open clusters with ages in the range ∼0.2–1 Gyr and initial metal mass fractions Z between ∼0.01 and ∼0.03 (Bastian et al. 2018; Cordoni et al. 2018; Marino et al. 2018) has somehow challenged this paradigm, given that extended TOs can be naturally explained by a range of ages amongst the cluster's stars (e.g. Mackey & Broby Nielsen 2007; Correnti et al. 2014). Further detailed studies of the extended TO phenomenon, which is seen also in CMDs of Magellanic Clouds' clusters younger than 2 Gyr (see e.g. Mackey et al. 2008; Piatti & Bastian 2016; Goudfrooij, Girardi & Correnti 2017, and references therein), strongly point to the effect of rotation (e.g. Bastian et al. 2018; Kamann et al. 2018, 2020, 2023) as the main culprit (see also D'Antona et al. 2023). In this case, stellar populations in individual open clusters might still be simple stellar populations, born with uniform age and initial chemical composition.

Very recently, our photometric multiband study of the main sequence (MS) of the open cluster M37 (Griggio et al. 2022b) has dis-

closed the presence of a sizeable initial chemical composition spread in the cluster (either a full metallicity range $\Delta[\mathrm{Fe/H}] \sim 0.15\,\mathrm{dex}$ or a helium mass fraction total range $\Delta Y \sim 0.10$). This result is independent of whether rotation or age spread is responsible for its observed extended TO, because it is based on an analysis of the lower MS, populated by stars with convective envelopes that are anyway slow rotators.

This result has important implications for our understanding of open cluster formation (see e.g. Clarke, Bonnell & Hillenbrand 2000) and the technique of 'chemical tagging' of Galactic field stars (e.g. Freeman & Bland-Hawthorn 2002; Hogg et al. 2016), especially if high resolution spectroscopic investigations of M37 will disclose that the chemical spread is due to an inhomogeneous initial metal content. Indeed, the basic idea of chemical tagging is that stars are born in unbound associations or star clusters (like open clusters) that disperse rapidly and over time they populate very different parts of the Milky Way phase space; stars of common birth origin should however be identifiable through their measured photospheric abundances, in the assumption that their birth cluster has a chemically homogeneous composition. It is therefore important to assess whether initial abundance spreads among the Galactic open clusters are a common phenomenon.

In this paper, we have investigated the poorly studied open cluster M38 that, like M37, displays in the *Gaia* Data Release 3 (DR3; Gaia Collaboration 2022) CMD, an MS broader than what is expected from photometric errors only. We have applied the same multiband technique developed for M37 that combines both *Gaia* and *Sloan*

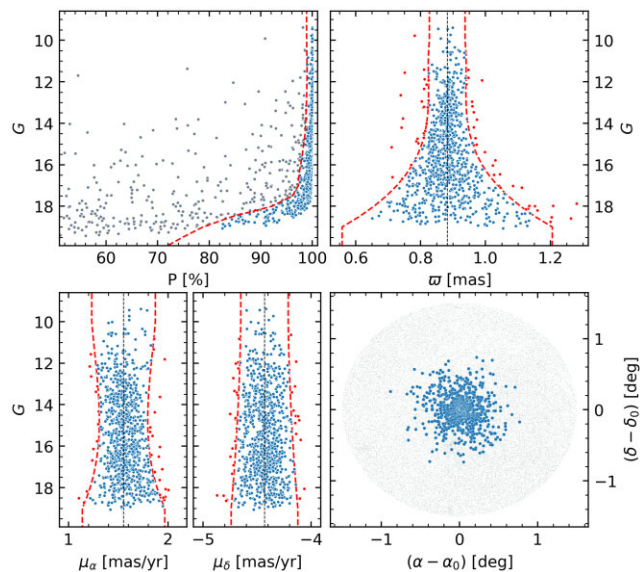★ E-mail: massimo.griggio@inaf.it

Figure 1. Cluster member selection. *Top left panel:* Membership probability for all the sources. In our analysis, we reject stars with $P < 50$ per cent. *Top right panel: G* magnitude versus parallax. In this case, we reject stars that fall outside the region bounded by the two red lines (red dots). The black dashed line denotes the median parallax. *Bottom left panel:* Proper motions versus *G* magnitude of all sources that passed the two previous selections. In this case, we kept the sources lying between the red dashed lines. *Bottom right panel:* Spatial distribution of the sources. The blue dots denote our selected members of M38.

photometry, to assess whether the broadening of the MS can be explained by differential reddening and binaries only, or whether a chemical abundance spread is also required.

The plan of the paper is as follows. Section 2 presents our membership analysis and the resulting *Gaia* DR3 CMD, and is followed by Section 3 that describes the complementary *Sloan* photometry used in this work. Section 4 describes the theoretical analysis of the MS width and Section 5 closes the paper with our conclusions.

2 THE *GAIA* COLOUR–MAGNITUDE DIAGRAM

The analysis of the CMD diagram of a star cluster requires a sample of member stars free from field sources contamination. To obtain such a sample, we have derived the membership probabilities for all the sources in the *Gaia* DR3 catalogue within a circle with a ~ 1.5 deg radius, centred on the cluster ($\alpha_0 = 82.167$, $\delta_0 = 35.824$; Tarricq et al. 2021).

The membership probabilities were computed following the approach described by Griggio & Bedin (2022), which relies on *Gaia* DR3 astrometry. Cluster members were selected by performing a series of cuts on the astrometric parameters, as displayed in Fig. 1. In the top left panel, we show the membership probability *P*: we applied a cut by-eye, following the profile of the bulk of sources with cluster membership at each magnitude (dashed red curve). This selection becomes less strict at fainter magnitudes, as the measurement errors increase and memberships become less certain. We then applied a cut on the parallax (top right) and proper motions (bottom left) distributions. The red lines were defined by the 68.27th percentile of the residuals around their median value in each 1-mag bin, multiplied by a factor of 2 (as in Griggio et al. 2022a). The bottom right panel shows the spatial distribution of the selected members.
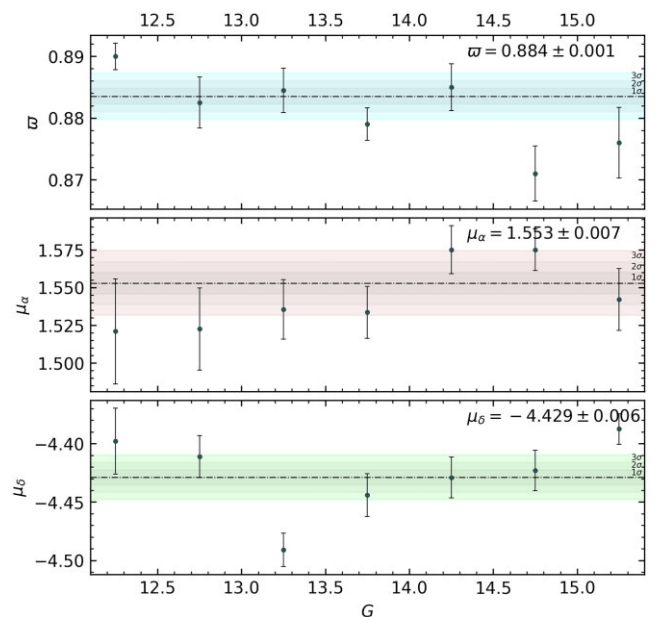

Figure 2. Mean values of the parallax and the components of the proper motion in each magnitude bin; the dash–dotted line denotes the overall weighted mean values, also reported at the top right corner of each panel (in mas and mas yr^{-1}, respectively) and in Table 1.

Table 1. M38's astrometric parameters estimated in this work.

μ_α (mas yr^{-1})	μ_δ (mas yr^{-1})	ϖ (mas)	Distance (pc)
1.553 ± 0.007	-4.429 ± 0.006	0.884 ± 0.001	1130 ± 50

The derived list of probable cluster members allowed us to estimate the cluster astrometric parameters; we followed the same procedure as in Griggio & Bedin (2022), by applying some quality cuts to the *Gaia* data, i.e.

  (i) `astrometric_excess_noise` < 0.25;
  (ii) `phot_bp_rp_excess_factor` < 1.4;
  (iii) `phot_proc_mode` $= 0$;
  (iv) `astrometric_gof_al` < 4;
  (v) $\sigma_\varpi/\varpi < 0.1$, $\sigma_{\mu_\alpha}/\mu_\alpha < 0.1$, and $\sigma_{\mu_\delta}/\mu_\delta < 0.1$.

With this selected sample of members, we have estimated the cluster's mean proper motion and parallax. The mean values in each magnitude interval are shown in Fig. 2, with the weighted average reported on the top right corner of each panel. The cluster parameters are also reported in Table 1.

The average parallax gives a distance *d* of 1132 ± 2 pc that, accounting for the parallax zero-point correction by Lindegren et al. (2021), becomes 1183 ± 2 pc. In the following, we consider this correction to represent a maximum error in the distance, hence $d = 1130 \pm 50$ pc. Our estimate is also in agreement, within the errors, with the distances given by Bailer-Jones et al. (2021), which provide a median value for M38 stars equal to 1186 ± 2 pc.

The CMD of the selected cluster members is shown in Fig. 3. The MS is very well defined and does not exhibit a clear extended TO. However, a detailed analysis of the TO region is hampered by the fact that there are only 40 MS stars with $G > 12$.

The metallicity of this cluster is not well determined, given that spectroscopic analyses of small samples of cluster stars have provided a range of [Fe/H] determinations between ~ -0.07 and

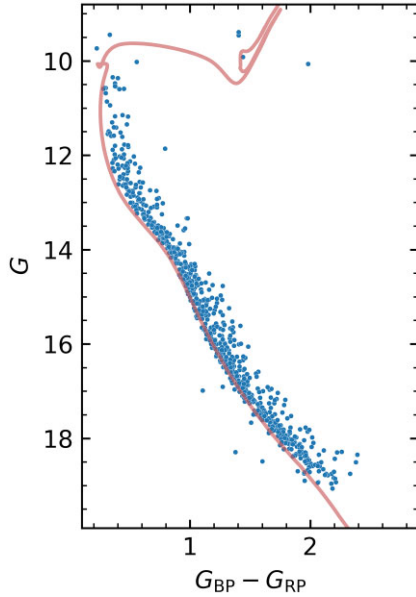**Figure 3.** *Gaia* CMD for the selected members of M38. The red line is a 300 Myr BaSTI-IAC isochrone, with [Fe/H] = 0.06, shifted by $E(B - V) =$ 0.26 and $d = 1130$ pc (see text for details).

~ -0.38, and $E(B - V)$ estimates range between ~ 0.25 and ~ 0.35 mag (see e.g. Subramaniam & Sagar 1999; Dias et al. 2002; Majaess, Turner & Lane 2007; Frinchaboy et al. 2013; Carrera R. et al. 2019; Donor et al. 2020; Zhong et al. 2020; Li et al. 2021).

In the same Fig. 3, we show for reference a 300 Myr[1] BaSTI-IAC (Hidalgo et al. 2018) solar scaled isochrone with [Fe/H] = 0.06, matched to the blue edge of the lower MS (see below and Section 4 for the definition of lower MS and its blue edge). We adopted the distance $d = 1130$ pc, and for the assumed metallicity we determined $E(B - V) = 0.26$ from the match to the lower MS colour, which can be considered to be the minimum value of the reddening, given the presence of differential reddening across the face of the cluster, as discussed later in Section 4. We employed extinction coefficients in the *Gaia* bands obtained from the relations given in the *Gaia* website.[2]

We tried also isochrones with lower [Fe/H] more in line with the uncertain spectroscopic estimates ([Fe/H] = −0.08 and −0.20 dex). After adjusting (actually increasing) $E(B - V)$ to match the blue edge of the lower MS and the isochrone age to approximately reproduce the observed brightness of the TO region, the fit of the upper MS was poorer when considering these subsolar metallicities.

We stress at this stage that – as for the case of M37 – the results of the analysis in Section 4 are insensitive to the exact values of the adopted isochrone metallicity, the cluster distance (within the adopted error bar), and the minimum value of $E(B - V)$, because of the differential nature of the technique applied.

2.1 The width of the MS

As discussed for M37 (Griggio et al. 2022b), if open clusters host single-metallicity populations, the observed colour width of the unevolved MS is expected to be set by the photometric error, the

---

[1]This value is consistent with the age of 302 Myr assigned to this cluster by Tarricq et al. (2021).
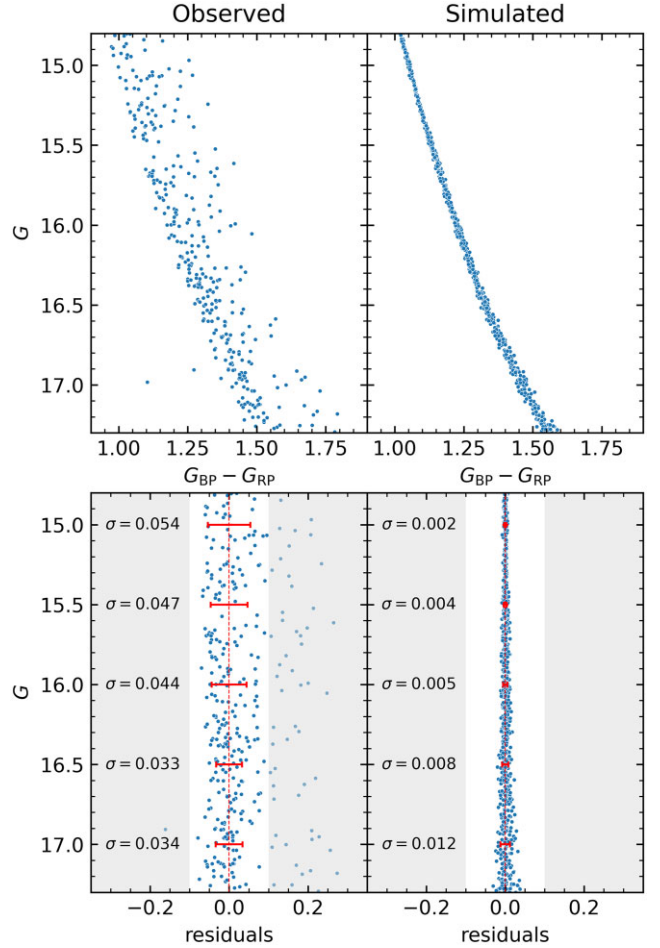[2]https://www.cosmos.esa.int/web/gaia/edr3-extinction-law

Figure 4. *Top panels*: Observed (left) and simulated (right) CMDs of the lower MS of M38. *Bottom panels*: Colour residuals as a function of the G magnitude around the observed (left) and the synthetic (right) CMD fiducials. The area shown in white contains the stars employed to compute the 1σ values of the dispersion of the residuals also shown in the two panels (see text for details).

presence of unresolved binaries with a range of values of the mass ratio q, and the differential reddening across the face of the cluster, if any. To verify this hypothesis in the case of M38, we have followed the same procedure detailed in Griggio et al. (2022b).

In brief, we first calculated an observed fiducial line of the unevolved MS in the G-magnitude range between 15.2 and 16.6 (denoted as lower MS from now on). According to the isochrone in Fig. 3, in this magnitude range the single star population covers a mass range between ~ 0.9 and $1.15 M_\odot$, approximately the same range as in our analysis of the lower MS of M37 (see Griggio et al. 2022b). We have calculated the fiducial line assuming that the observed MS is populated just by single stars all with the same initial metallicity, as described in Griggio et al. (2022b). Synthetic stars have been then distributed with uniform probability along this fiducial; each synthetic magnitude has been then perturbed by a photometric error obtained by randomly sampling a Gaussian probability distribution with zero mean and a standard deviation set to the median error at the corresponding G magnitude, taking advantage of the individual errors from the *Gaia* DR3 catalogue. Fig. 4 (top panels) compares the observed CMD (left) with the simulated counterpart (right) in the selected magnitude range and the colour residuals around the fiducial line as a function of G (bottom

Table 2. Log of the observations.

Filter	N_{exp}	t_{exp}	Seeing	Airmass
u	57	400 s	2.25 arcsec	1.08
g	57	400 s	2.20 arcsec	1.09
i	57	400 s	2.17 arcsec	1.07
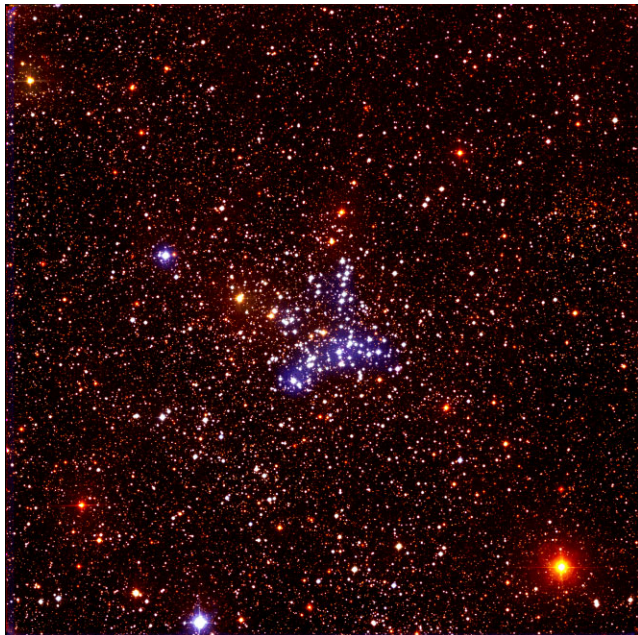
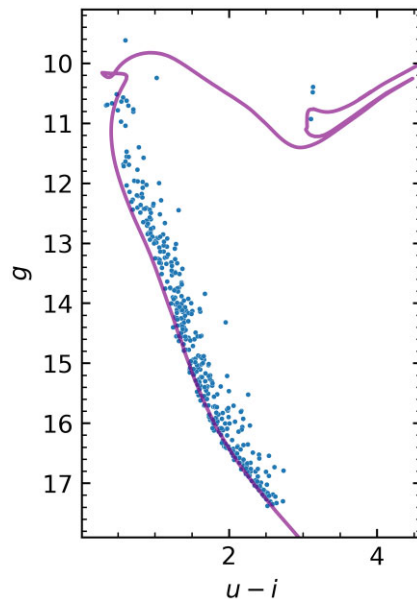**Figure 5.** Three colour stack of the Asiago Schmidt Telescope data. The field of view is approximately $1 \times 1 \, \mathrm{deg}^2$.

Figure 6. CMD in the *Sloan* filters for M38 members. The purple line is the same isochrone of Fig. 3 (see text for details).

panels). We also show the values of the colour dispersion around the fiducial values at varying magnitudes in both CMDs. They have been computed as the 68.27th percentile of the distribution of the residuals around zero.

Notice that we have discarded objects with the position in the CMD consistent with being unresolved binaries with mass ratio $q > 0.7$ (according to the adopted isochrone) when we calculated the dispersion of the residuals from the observations. But even neglecting these objects, it is clear from Fig. 4 that the simulated stars display a much narrower distribution around the fiducial line than the observations.

To assess the origin of the colour spread of the observed CMD, we employed an auxiliary photometry in the *Sloan ugi* filters – described in the following section – and applied in Section 4, the same technique developed in Griggio et al. (2022b).

3 *SLOAN* OBSERVATIONS AND DATA REDUCTION

The data were collected with the Asiago Schmidt telescope between 2022 October 2 and November 15. We obtained a set of 57 images in the *Sloan*-like filters *ugi*, with an exposure time of 400 s. The images were dithered to mitigate the effect of bad pixels and cosmic rays, and covered a total area of about 1 deg². The observation log is reported in Table 2. A three colour stack of the field of view is shown in Fig. 5, where we used the *u* filter for the blue colour, *g* for the green, and *i* for the red colour.

To measure position and flux of the sources in this data set, we followed the same approach as in Griggio et al. (2022a). Briefly, we first derived a grid of 9×9 empirical point spread functions (PSFs) for each image considering bright, isolated, and unsaturated sources, by using the software originally developed by Anderson et al. (2006). The grid is necessary to account for spatial variations of the PSF across the CCD. We then proceeded by measuring the position and flux of individual sources in each image with the appropriate local PSF, obtained by a bilinear interpolation between the four nearest PSFs in the grid, using the software described by Anderson et al. (2006). This routine goes through a series of iterations, finding and measuring progressively fainter sources, until it reaches a specified level about the sky background noise. The software outputs a catalogue with positions and instrumental magnitudes for each image.

We transformed the positions and magnitudes of each catalogue to the reference system defined by the first image in each filter (namely, SC233176, SC233182, and SC233188). Finally, we cross identified the sources and produced a catalogue containing the averaged positions and magnitudes for all the stars measured in at least five exposures. These catalogues were matched with the *Gaia* one, to have *Sloan* magnitudes for all the *Gaia* sources detected with the Schmidt telescope.

The instrumental magnitudes have been calibrated as in Griggio et al. (2022a) exploiting the IGAPS catalogue (Monguió et al. 2020). We cross identified our sources with those in the IGAPS catalogue and derived the coefficients of the relation $m_{cal} = m_{instr} + a(g_{instr} - i_{instr}) + b$ with a linear fit.

The CMD of member stars in the *ugi* filters is shown in Fig. 6, together with the same isochrone (purple line) of Fig. 3, employing the same distance and reddening, and the extinction law from the NASA/IPAC infrared science archive[3] for the *Sloan* filters.

[3] https://irsa.ipac.caltech.edu/applications/DUST/

Figure 8. $\Delta_{GBR}-\Delta_{Gui}$ diagram for the lower MS stars. The lines show the directions along which stars would be displaced by differential reddening, unresolved binaries, and initial chemical spread (see text for details).
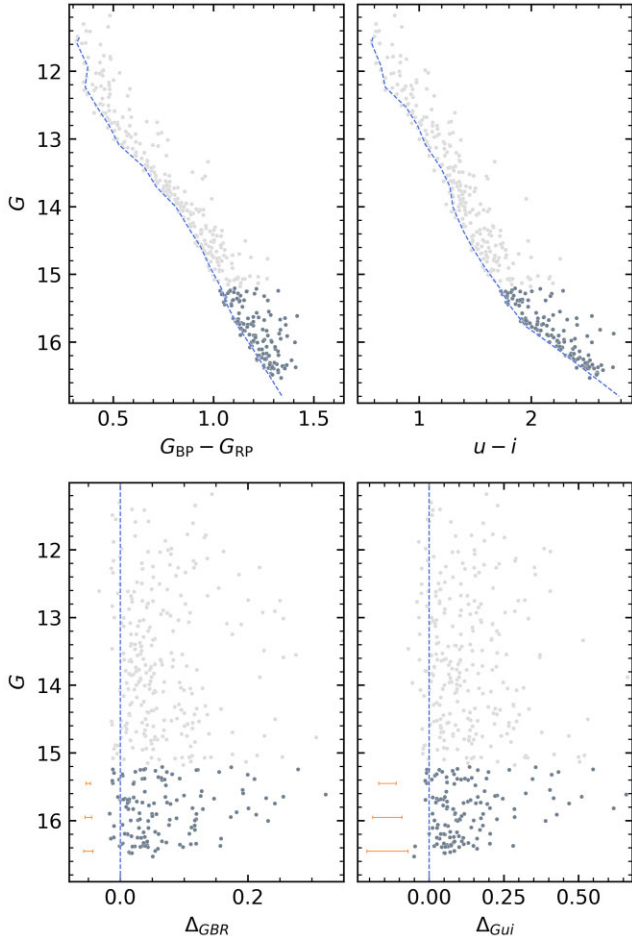
Figure 7. *Top panels*: Cluster $G-(G_{BP}-G_{RP})$ and $G-(u-i)$ diagrams. The blue dashed line denotes the MS blue edge fiducial. The lower MS stars considered in our analysis are displayed in dark grey. *Bottom panels*: $G-\Delta_{GBR}$ and $G-\Delta_{Gui}$ diagrams (see text for details). Along the left-hand side of each panel, we display the median $\pm 1\sigma$ colour error for three representative G magnitudes, as estimated from the individual catalogues.

4 THE BROADENING OF THE LOWER MS

To investigate in detail the origin of the broadening of the lower MS, we followed the same technique described in Griggio et al. (2022b). We considered stars in the *Gaia* CMD with G between 15.2 and 16.6 (we have a total of 132 stars in this magnitude range) and combined the photometry in the *Gaia* filters with the corresponding u and i magnitudes to build a differential colour–colour diagram, as summarized below.

We have defined an MS blue fiducial in both the $G-(G_{BP}-G_{RP})$ and $G-(u-i)$ diagrams as described in Griggio et al. (2022b) and for each observed star we have computed, in both $G-(G_{BP}-G_{RP})$ and $G-(u-i)$ diagrams, the difference between its colour and the colour of the corresponding blue fiducial at the star G magnitude. These quantities are denoted as Δ_{GBR} and Δ_{Gui}, respectively (see Fig. 7).

We then plotted these colour differences in the $\Delta_{GBR}-\Delta_{Gui}$ diagram shown Fig. 8. As for the case of M37, the lower MS stars are distributed along a well-defined sequence that starts around the coordinates (0, 0) – corresponding to the stars lying on the blue fiducials – and stretches towards increasingly positive values (denoting stars increasingly redder than the fiducials) with the
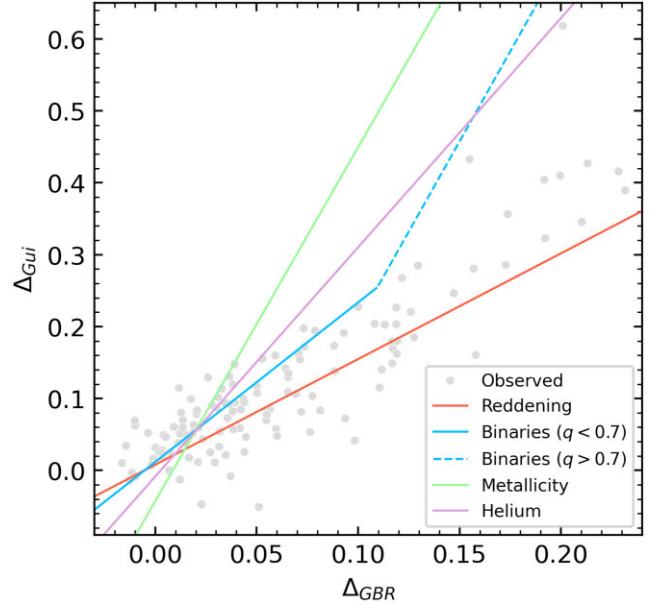
quantity Δ_{Gui} increasing faster than Δ_{GBR}. These colour spreads cannot arise from (underestimated) random photometric errors only, because in this case they would be distributed without a correlation between Δ_{Gui} and Δ_{GBR}.

In the same figure, together with the data, we show the reddening vector, calculated using the extinction laws for the *Gaia* and *Sloan* filters referenced above. We also plot the vector corresponding to the predicted position of binaries with varying mass ratio q (blue) and the range of colours spanned by isochrones with increasing [Fe/H] and increasing Y (green and magenta). These vector have been calculated as described by Griggio et al. (2022b) for M37, using as reference the isochrone in Fig. 3, and the corresponding values of d and $E(B-V)$ (see Section 2). In this figure, we display the effect of binaries as a two-slope sequence, because it is a better representation of the trend predicted by synthetic stellar populations, compared to a single slope as shown in Griggio et al. (2022b).

The figure shows that, in the case of M38, the distribution of the stars' colours in this diagram follows a trend consistent with a combination of differential reddening across the face of the cluster and the presence of unresolved binaries with varying q. There is no need to invoke the presence of a range of [Fe/H] or Y among the clusters' stars. This is at odds with the case of M37, where binaries and differential reddening produced too shallow slopes in this diagram, compared to the observations (see the Appendix A for a comparison of the CMDs and $\Delta_{GBR}-\Delta_{Gui}$ diagrams of M37 and M38).

Fig. 9 shows a synthetic sample of stars – computed as in Griggio et al. (2022b), using isochrone, distance, and reference reddening previously discussed – compared to observations in the $\Delta_{GBR}-\Delta_{Gui}$ diagram. The purpose of this comparison is just to see how binaries and differential reddening only can account qualitatively for the observed distribution of lower MS stars in this diagram.

The full synthetic sample of 50 000 objects includes observational errors in both the *Gaia* and *Sloan* magnitudes, and contains a 70 per cent fraction of unresolved binaries with mass ratios q distributed as $f(q) \propto q^{-0.6}$ following Malofeeva, Seleznev & Carraro (2022). It
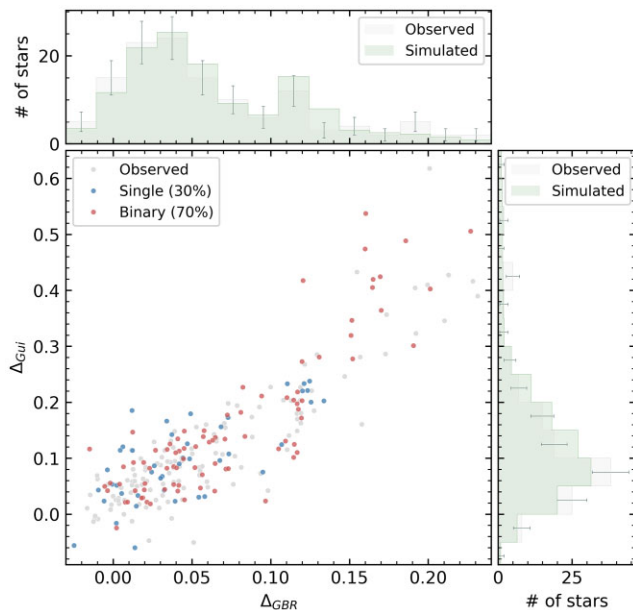
Figure 9. Comparison of the distribution of the synthetic population (including binaries and a spread of $E(B-V)$ to account for differential reddening – see text for details) and the observed cluster stars (grey filled circles) in the $\Delta_{GBR}-\Delta_{Gui}$ diagram. Synthetic single and unresolved binary stars are shown in blue and red respectively. Histograms of the observed (with Poisson error bars) and simulated number counts along the two axes are also shown (see text for details).

is worth pointing out that in the case of assuming a flat probability distribution for q, the same results described below are obtained with a 10–15 per cent binary fraction.

We display here one random subset of the full sample, containing the same number of objects as the observations. The figure also shows along the horizontal and vertical axis a comparison of the number distributions of synthetic and observed stars as a function of the two quantities Δ_{GBR} and Δ_{Gui}, respectively. When calculating these histograms, we have considered the full sample of synthetic stars and rescaled the derived histograms to have the same total number of objects as observed.

The contribution of differential reddening has been accounted for by using a double Gaussian distribution; only in this way, we are able to reproduce the clump of stars clearly visible in the Δ_{GBR} histogram at $\Delta_{GBR} \sim 0.12$. The parameters of the distributions have been adjusted to roughly reproduce the observed trends of the number distributions in both Δ_{GBR} and Δ_{Gui}, because we could not determine a reliable differential reddening map for M38 using the technique described by, e.g. Sarajedini et al. (2007), given the relatively low number of objects. The first Gaussian accounts for a random sample of ~ 80 per cent of the synthetic stars (both single and binary objects) and is centred on $E(B-V) = E(B-V)_{\rm ref} + 0.04$, with $\sigma = 0.033$ mag, where $E(B-V)_{\rm ref} = 0.26$. The second Gaussian distribution is centred on $E(B-V) = E(B-V)_{\rm ref} + 0.15$, with $\sigma = 0.01$ mag, and accounts for the remaining objects in the synthetic sample.

It is remarkable how this synthetic sample, which includes just unresolved binaries and the effect of differential reddening, follows nicely the observed trend in this diagram. Also, the observed number distribution across the diagram can be followed quite well by using two simple Gaussian $E(B-V)$ distributions and the power-law q distribution determined by Malofeeva et al. (2022). This shows that there is no need to invoke a chemical abundance spread to explain the width of the lower MS in this cluster.

We have then repeated the analysis previously described considering this time stars in the brighter G magnitude range between 12.5 and 14, corresponding to single star masses between ~ 1.5 and $\sim 2.2\,{\rm M_\odot}$. Using the same binary fraction, q and $E(B-V)$ distributions of the previous comparison, we have found the same agreement of the number distributions of synthetic and observed stars across the $\Delta_{GBR}-\Delta_{Gui}$ diagram as in Fig. 9.

The same comparison could not be performed for objects in the TO region of the CMD, because of the small sample of cluster stars in this magnitude range (see Section 2).

5 SUMMARY AND CONCLUSIONS

We have employed the accurate *Gaia* DR3 photometry and astrometry of the poorly studied open cluster M38 to select *bona fide* members and determine the cluster distance and mean proper motion. The *Gaia* CMD does not show an obvious extended TO despite the cluster being ~ 300 Myr old, but the number of stars in the TO region is too small to investigate quantitatively this matter. The unevolved MS is broader than expected from photometric errors only and to determine the origin of this broadening we have applied the same technique developed to study the open cluster M37 (Griggio et al. 2022b), making use of auxiliary photometry in the *Sloan* system to build a differential colour–colour diagram of the lower MS from combinations of *Gaia* and *Sloan* magnitudes.

We employed synthetic stellar populations to reproduce the observed trend of M38 stars in this diagram, and found that the observed MS colour spread can be explained simply by the combined effect of differential reddening and unresolved binaries. There is no need to include a spread of initial chemical composition (either metals or helium) as instead necessary to explain the same differential colour–colour diagram for the lower MS of M37.

Despite having similar total masses (estimated total masses on the order of 1000–1500 $\rm M_\odot$, mutually consistent within the associated errors, see Piskunov et al. 2008) and metallicities different on average by no more than at most a factor 2 and 3, the open clusters M38 and M37 seem to host stellar populations with a clear difference: single versus multiple chemical compositions. The origin of this difference is unknown and we do not know as well whether the chemical abundance spread found photometrically in M37 is a feature common to many more open clusters, and if there is any connection with the extended TO phenomenon.

Further photometric investigations like ours, as well as accurate differential spectroscopic analyses on a large sample of open clusters are necessary to shed light on this phenomenon and its implications for cluster formation and the use of open clusters and chemical tagging to study the formation and evolution of the Galactic disc.

DATA AVAILABILITY

The isochrones employed in this study can be retrieved at http://basti-iac.oa-abruzzo.inaf.it, but for the helium enhanced isochrones, which are available upon request.

The calibrated photometry and astrometry employed in this article is released as supplementary online material and available at https://web.oapd.inaf.it/bedin/files/PAPERs_eMATERIALs/M38_ugiSchmidt/, along with an atlas. The same catalogue also conveniently lists the *Gaia* DR3 photometry, astrometry, and source ID, when available.

REFERENCES

Anderson J., Bedin L. R., Piotto G., Yadav R. S., Bellini A., 2006, A&A, 454, 1029

Bailer-Jones C. A. L., Rybizki J., Fouesneau M., Demleitner M., Andrae R., 2021, AJ, 161, 147

Bastian N., Kamann S., Cabrera-Ziri I., Georgy C., Ekström S., Charbonnel C., de Juan Ovelar M., Usher C., 2018, MNRAS, 480, 3739

Carrera R. et al., 2019, A&A, 623, A80

Clarke C. J., Bonnell I. A., Hillenbrand L. A., 2000, in Mannings V., Boss A. P., Russell S. S., eds, Protostars and Planets IV. Univ. Arizona Press, Tucson, AZ, p. 151

Cordoni G., Milone A. P., Marino A. F., Di Criscienzo M., D'Antona F., Dotter A., Lagioia E. P., Tailo M., 2018, ApJ, 869, 139

Correnti M., Goudfrooij P., Kalirai J. S., Girardi L., Puzia T. H., Kerber L., 2014, ApJ, 793, 121

D'Antona F. et al., 2023, MNRAS, 521, 4462

Dias W. S., Alessi B. S., Moitinho A., Lépine J. R. D., 2002, A&A, 389, 871

Donor J. et al., 2020, AJ, 159, 199

Freeman K., Bland-Hawthorn J., 2002, ARA&A, 40, 487

Frinchaboy P. M. et al., 2013, ApJ, 777, L1

Gaia Collaboration et al., 2022, preprint (arXiv:2208.00211)

Goudfrooij P., Girardi L., Correnti M., 2017, ApJ, 846, 22

Griggio M., Bedin L. R., 2022, MNRAS, 511, 4702

Griggio M. et al., 2022a, MNRAS, 515, 1841

Griggio M., Salaris M., Cassisi S., Pietrinferni A., Bedin L. R., 2022b, MNRAS, 516, 3631

Hidalgo S. L. et al., 2018, ApJ, 856, 125

Hogg D. W. et al., 2016, ApJ, 833, 262

Kamann S. et al., 2018, MNRAS, 480, 1689

Kamann S. et al., 2020, MNRAS, 492, 2177

Kamann S. et al., 2023, MNRAS, 518, 1505

Li C.-Y. et al., 2021, Res. Astron. Astrophys., 21, 068

Lindegren L. et al., 2021, A&A, 649, A4

Mackey A. D., Broby Nielsen P., 2007, MNRAS, 379, 151

Mackey A. D., Broby Nielsen P., Ferguson A. M. N., Richardson J. C., 2008, ApJ, 681, L17

Majaess D. J., Turner D. G., Lane D. J., 2007, PASP, 119, 1349

Malofeeva A. A., Seleznev A. F., Carraro G., 2022, AJ, 163, 113

Marino A. F., Milone A. P., Casagrande L., Przybilla N., Balaguer-Núñez L., Di Criscienzo M., Serenelli A., Vilardell F., 2018, ApJ, 863, L33

Monguió M. et al., 2020, A&A, 638, A18

Piatti A. E., Bastian N., 2016, A&A, 590, A50

Piskunov A. E., Schilbach E., Kharchenko N. V., Röser S., Scholz R.-D., 2008, A&A, 477, 165

Sarajedini A. et al., 2007, AJ, 133, 1658

Subramaniam A., Sagar R., 1999, AJ, 117, 937

Tarricq Y. et al., 2021, A&A, 647, A19

Zhong J., Chen L., Wu D., Li L., Bai L., Hou J., 2020, A&A, 640, A127

SUPPORTING INFORMATION

Supplementary data are available at *MNRAS* online.

CATALOG.dat

Please note: Oxford University Press is not responsible for the content or functionality of any supporting materials supplied by the authors. Any queries (other than missing material) should be directed to the corresponding author for the article.

APPENDIX A: COMPARISON OF M37 AND M38 DIAGRAMS

We present here a comparison of the *Gaia* CMD and the $\Delta_{GBR} - \Delta_{Gui}$ diagrams of M37 and M38. The top panels of Fig. A1 show the CMDs of our M37 (left) and M38 (right) *bona fide* members, highlighting in a darker shade of grey the sources employed in the analysis of the width of the MS. The bottom panels display the $\Delta_{GBR} - \Delta_{Gui}$ diagrams of both cluster's lower MS. The points are clearly distributed along different slopes in the two diagrams; in particular, we also notice the behaviour of high-q binaries ($\Delta_{GBR} \gtrsim 0.1$) in the case of M37, which are distributed along a steeper line, while M38 stars in the same region follow a shallower direction.
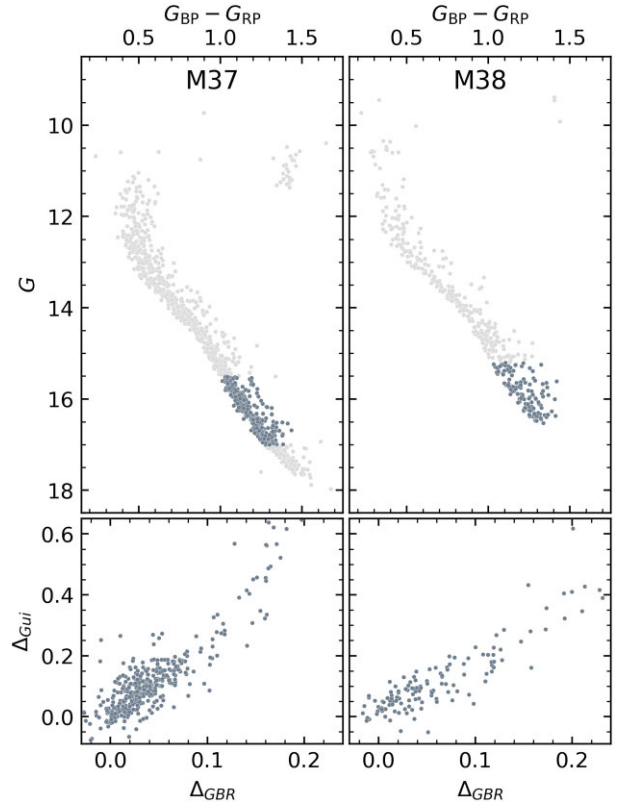

Figure A1. Comparison of M37 and M38 CMDs and $\Delta_{GBR} - \Delta_{Gui}$ diagrams.

This paper has been typeset from a TEX/LATEX file prepared by the author.